

Multi-valley superconductivity in ion-gated MoS₂ layers

Erik Piatti, Domenico De Fazio, Dario Daghero, Srinivasa Reddy
Tamalampudi, Duhee Yoon, Andrea C Ferrari, and Renato Gonnelli

Nano Lett., **Just Accepted Manuscript** • DOI: 10.1021/acs.nanolett.8b01390 • Publication Date (Web): 27 Jun 2018

Downloaded from <http://pubs.acs.org> on July 4, 2018

Just Accepted

“Just Accepted” manuscripts have been peer-reviewed and accepted for publication. They are posted online prior to technical editing, formatting for publication and author proofing. The American Chemical Society provides “Just Accepted” as a service to the research community to expedite the dissemination of scientific material as soon as possible after acceptance. “Just Accepted” manuscripts appear in full in PDF format accompanied by an HTML abstract. “Just Accepted” manuscripts have been fully peer reviewed, but should not be considered the official version of record. They are citable by the Digital Object Identifier (DOI®). “Just Accepted” is an optional service offered to authors. Therefore, the “Just Accepted” Web site may not include all articles that will be published in the journal. After a manuscript is technically edited and formatted, it will be removed from the “Just Accepted” Web site and published as an ASAP article. Note that technical editing may introduce minor changes to the manuscript text and/or graphics which could affect content, and all legal disclaimers and ethical guidelines that apply to the journal pertain. ACS cannot be held responsible for errors or consequences arising from the use of information contained in these “Just Accepted” manuscripts.



Multi-Valley Superconductivity In Ion-Gated MoS₂ Layers

Erik Piatti,^{†,¶} Domenico De Fazio,^{‡,¶} Dario Daghero,[†] Srinivasa Reddy Tamalampudi,[‡] Duhee Yoon,[‡] Andrea C. Ferrari,^{*,‡} and Renato S. Gonnelli[†]

*Department of Applied Science and Technology, Politecnico di Torino, 10129 Torino, Italy, and
Cambridge Graphene Centre, University of Cambridge, Cambridge CB3 0FA, UK*

E-mail: acf26@eng.cam.ac.uk

KEYWORDS: Transition metal dichalcogenides, ionic gating, superconductivity, electron-phonon coupling, Raman spectroscopy, Lifshitz transitions

Abstract

Layers of transition metal dichalcogenides (TMDs) combine the enhanced effects of correlations associated with the two-dimensional limit with electrostatic control over their phase transitions by means of an electric field. Several semiconducting TMDs, such as MoS₂, develop superconductivity (SC) at their surface when doped with an electrostatic field, but the mechanism is still debated. It is often assumed that Cooper pairs reside only in the two electron pockets at the K/K' points of the Brillouin Zone. However, experimental and theoretical results suggest that a multi-valley Fermi surface (FS) is associated with the SC state, involving 6 electron pockets at the Q/Q' points. Here, we perform low-temperature transport measurements in ion-gated MoS₂ flakes. We show that a fully multi-valley FS is associated with the SC onset.

*To whom correspondence should be addressed

[†]Department of Applied Science and Technology, Politecnico di Torino, 10129 Torino, Italy

[‡]Cambridge Graphene Centre, University of Cambridge, Cambridge CB3 0FA, UK

[¶]These authors contributed equally to this work.

1
2
3 The Q/Q' valleys fill for doping $\gtrsim 2 \cdot 10^{13} \text{ cm}^{-2}$, and the SC transition does not appear until the
4 Fermi level crosses both spin-orbit split sub-bands Q_1 and Q_2 . The SC state is associated with
5 the FS connectivity and promoted by a Lifshitz transition due to the simultaneous population
6 of multiple electron pockets. This FS topology will serve as a guideline in the quest for new
7 superconductors.
8
9
10
11
12

13
14 Transition metal dichalcogenides (TMDs) are layered materials with a range of electronic prop-
15 erties. Depending on chemical composition, crystalline structure, number of layers (N), doping,
16 and strain, different TMDs can be semiconducting, metallic and superconducting.¹ Amongst semi-
17 conducting TMDs, MoS_2 , MoSe_2 , WS_2 and WSe_2 have sizeable bandgaps in the range $\sim 1\text{-}2\text{eV}$.²
18 When exfoliated from bulk to single layer (1L), they undergo an indirect-to-direct gap transition,²⁻⁴
19 offering a platform for electronic and optoelectronic applications,^{1,2,5} such as transistors,⁶⁻⁸ pho-
20 todetectors,⁹⁻¹² modulators¹³ and electroluminescent devices.^{14,15}
21
22
23
24
25
26

27
28 For all TMDs with 2H crystal structure, the hexagonal Brillouin Zone (BZ) features high-
29 symmetry points Γ , M, K and K',^{4,16} Fig.1a. The minima of the conduction band fall at K, K',
30 as well as at Q, Q', approximately half-way along the Γ -K(K') directions,^{4,16} Fig.1a. In absence
31 of an out-of-plane electric field, the relative position of Q and Q' depends on N and strain.^{4,16,20}
32 The global minimum of the conduction band sits at K/K' in 1L- MoS_2 and at Q/Q' in few layer
33 (FL)- MoS_2 with $N \geq 4$.⁴ When an electric field is applied perpendicular to the MoS_2 plane, in-
34 version symmetry is broken and the global minimum of the conduction band is shifted to K/K'
35 in any FL- MoS_2 ,¹⁶ Figs.1b-d. The valleys at K/K' and at Q/Q' are characterized by a different
36 electron-phonon coupling (EPC)²¹ and, when inversion symmetry is broken, by a different spin-
37 orbit coupling (SOC).²² In particular, both EPC and SOC are larger in the Q/Q' valleys.^{21,22}
38
39
40
41
42
43
44
45
46
47

48 The field-effect transistor (FET) architecture is ideally suited to control the electronic proper-
49 ties of 1L flakes, as it simultaneously provides an electrostatic control of the transverse electric
50 field and the carrier density. In the electric-double-layer (EDL) technique,²³ the standard solid
51 gate dielectric is replaced by an ionic medium, such as an ionic liquid or electrolyte. In this con-
52 figuration, the EDL that forms at the ionic liquid/electrode interfaces supports electric fields in
53
54
55
56
57
58
59
60

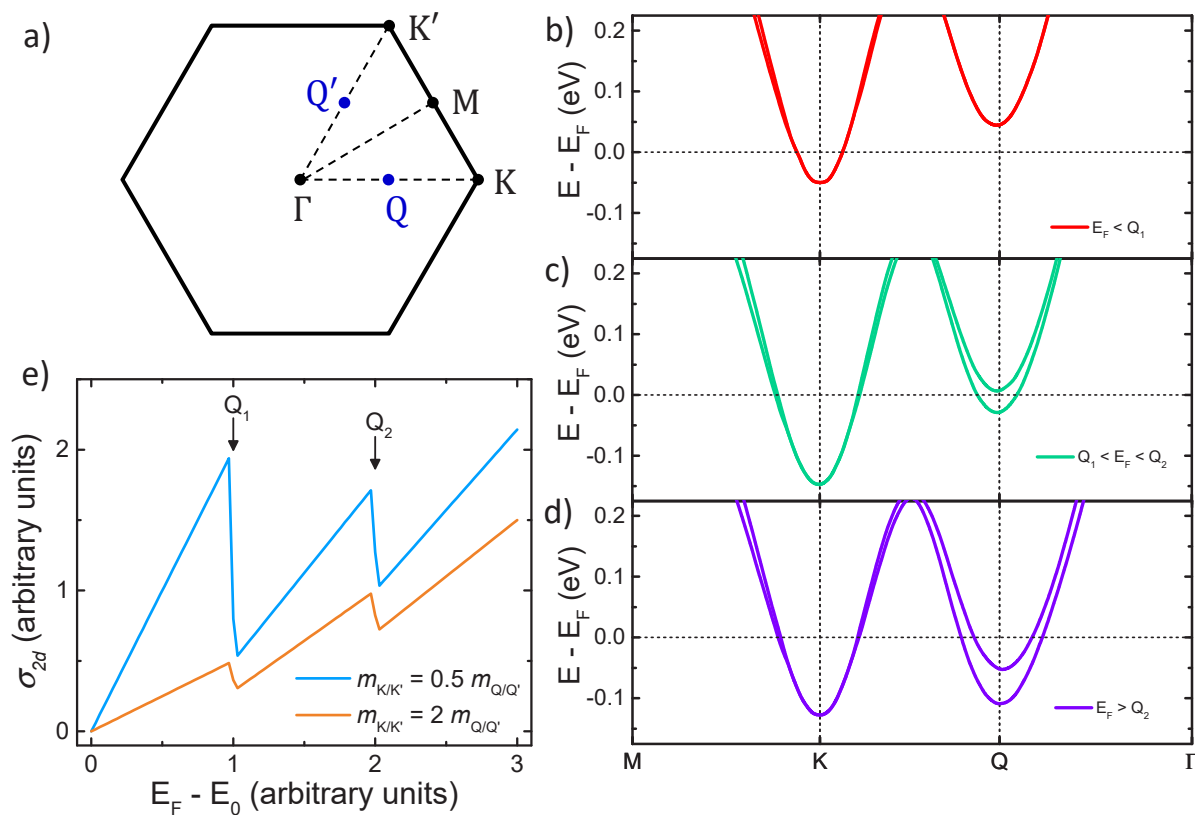


Figure 1: a) BZ for the 2H crystal structure. High symmetry points Γ , M, K, K', and points Q and Q' are indicated. b-d) 3L-MoS₂ band structure for 3 doping values. The bands are adapted from Ref. 16, and were obtained by Density Functional Theory (DFT) calculations using the Quantum ESPRESSO package¹⁷ in the field-effect transistor configuration.¹⁸ The valleys at K/K' have two spin-orbit split sub-bands, with splitting much smaller than at Q/Q', not seen in this scale. e) Schematic dependence of σ_{2d} for increasing E_F above the global energy minimum of the conduction band, E_0 , at T=0, for 2 ratios of the effective masses in the K/K' and Q/Q' electron pockets ($m_{K/K'}$ and $m_{Q/Q'}$). Curves are calculated using Eq.6 of Ref. 19 and setting a total degeneracy of 4 for the K/K' pockets, 6 for the first Q/Q' pocket (Q_1), and 6 for the second Q/Q' pocket (Q_2); physical constants and energy separations are set to unity.

1
2
3 excess of $\sim 10\text{MV/cm}$,²⁴ corresponding to surface carrier densities $n_{2d} \gtrsim 10^{14}\text{cm}^{-2}$.²⁴ Ionic-liquid
4 gating has been used to tune the Fermi level, E_F , in TMDs and explore transport at different carrier
5 concentrations.^{25–29} The vibrational properties of TMDs can also be controlled by means of the
6 EDL technique, as suggested by gate-induced softening of Raman-active modes in 1L-MoS₂,³⁰
7 while the opposite is observed in gated 1L³¹ and two-layer (2L)³² graphene. Ref. 26 reported a
8 gate-induced superconducting state at the surface of liquid-gated MoS₂ flakes with $N \gtrsim 25$,²⁶ while
9 Ref. 33 detected this down to $N=1$.

10
11
12
13
14
15
16
17 Most of these results have been interpreted in terms of the population of the conduction band
18 minima at K/K',^{26,34–36} which are global minima in both 1L-MoS₂^{3,21} and electrostatically-doped
19 FL-MoS₂,^{16,26,34,35} Fig.1b. Theoretical investigations however suggested that the population of
20 the high-energy minima at Q/Q' may have an important role in determining the properties of gated
21 MoS₂ flakes, by providing contributions both to EPC^{16,21} and SOC.^{22,37} Ref. 21 predicted that
22 when the Q/Q' valleys of 1L-MoS₂ are populated (Fig.1c,d), EPC strongly increases (from ~ 0.1
23 to ~ 18), leading to a superconducting transition temperature $T_c \sim 20\text{K}$ for a doping level $x =$
24 0.18 electrons(e^-)/unit cell (corresponding to $E_F = 0.18 \pm 0.02\text{eV}$ at K/K' and $0.08 \pm 0.02\text{eV}$ at
25 Q/Q')¹⁶). However, Ref. 33 measured $T_c \sim 2\text{K}$ for $x \sim 0.09 \div 0.17$ e^- /unit cell in e^- -doped 1L-
26 MoS₂. This mismatch may be associated with the contribution of e^-e^- interactions, whose role
27 in the determination of T_c is still under debate.^{38,39} Overall, the agreement between the model of
28 Ref. 21 and the trend of T_c with e^- doping in Ref. 26 suggests that the mechanism of Ref. 21 for
29 EPC enhancement when the Q/Q' valleys are crossed may also hold for FL-MoS₂.

30
31
32
33
34
35
36
37
38
39
40
41
42
43 Inversion symmetry can be broken in MoS₂ either by going to the 1L limit,²¹ or by applying
44 a transverse electric field.^{40,41} This leads to a finite SOC,^{40,41} which lifts the spin degeneracy in
45 the conduction band and gives rise to two spin-orbit-split sub-bands in each valley,^{16,40} as shown
46 in Fig.1b-d for FL-MoS₂. When the system is field-effect doped, the inversion symmetry breaking
47 increases with increasing transverse electric field,^{34,36} due to the fact that induced e^- tend to
48 become more localized within the first layer.^{34,36,38} Hence, the SOC and the spin-orbit splitting
49 between the bands increase as well, as was calculated in Ref. 16.

1
2
3 When combined to the gate-induced SC state,⁴¹ this can give rise to interesting physics, such
4 as spin-valley locking of the Cooper pairs³⁵ and 2d Ising superconductivity (SC)³⁴ with a non-
5 BCS-like energy gap,⁴² suggested to host topologically non-trivial SC states.^{38,43,44} Refs. 16,22
6 predicted SOC and spin-orbit splitting between sub-bands to be significantly stronger for the Q/Q'
7 valleys than for K/K', thus supporting spin-valley locking at Q/Q' as well.³⁷ A dominant contri-
8 bution of the Q/Q' valleys in the development of the SC state would be consistent with the high
9 ($\gtrsim 50$ T) in-plane upper critical field, H_{c2}^{\parallel} , observed in ion-gated MoS₂^{34,35} and WS₂.⁴⁵ The H_{c2}^{\parallel}
10 enhancement is caused by locking of the spin of the Cooper pairs in the out-of-plane direction in a
11 2d superconductor in the presence of finite SOC, and is therefore promoted by increasing the SOC.
12 However, H_{c2}^{\parallel} for MoS₂ and WS₂ is higher than in metallic TMD Ising superconductors (such as
13 NbSe₂ and TaS₂), where $H_{c2}^{\parallel} \lesssim 30$ T,⁴⁶ despite the SOC in the K/K' valleys being much smaller
14 (~ 3 meV for MoS₂⁴⁰). Spin-valley locking in the Q/Q' valleys may thus explain this apparent
15 inconsistency in the physics of ion-gated semiconducting TMDs under magnetic field.
16
17
18
19
20
21
22
23
24
25
26
27
28

29 From the experimental point of view, the possible multi-valley character of transport in gated
30 TMDs is currently debated. Refs. 36,37,47 measured the Landau-level degeneracy at moderate
31 $n_{2d} \sim 10^{12} - 10^{13} \text{cm}^{-2}$, finding it compatible with a carrier population in the Q/Q' valleys. How-
32 ever, Ref. 36 argued that this would be suppressed for larger $n_{2d} \gtrsim 10^{13} \text{cm}^{-2}$, typical of ion-gated
33 devices and mandatory for the emergence of SC) due to stronger confinement within the first
34 layer.³⁶ In contrast, angle-resolved photoemission spectroscopy in surface-Rb-doped TMDs⁴⁸
35 highlighted the presence of a non-negligible spectral weight at the Q/Q' valleys only for $n_{2d} \gtrsim$
36 $8 \cdot 10^{13} \text{cm}^{-2}$ in the case of MoS₂. Thus, which valleys and sub-bands are involved in the gate-
37 induced SC state still demands a satisfactory answer.
38
39
40
41
42
43
44
45
46

47 Here we report multi-valley transport and SC at the surface of liquid-gated FL-MoS₂. We use
48 a dual-gate geometry to tune doping across a wide range of $n_{2d} \sim 5 \cdot 10^{12} - 1 \cdot 10^{14} \text{cm}^{-2}$, induce
49 SC, and detect characteristic “kinks” in the transconductance. These are non-monotonic features
50 that emerge in the n_{2d} -dependence of the low-temperature (T) conductivity when E_F crosses the
51 high-energy sub-bands,¹⁹ irrespectively of their specific effective masses, Fig.1e. We show that
52
53
54
55
56
57
58
59
60

1
2
3 the population of the Q/Q' valleys is fundamental for the emergence of SC. The crossing of the
4 first sub-band Q₁ (Fig.1c) occurs at small $n_{2d} \lesssim 2 \cdot 10^{13} \text{cm}^{-2}$, implying that multi-valley transport
5 already occurs in the metallic phase over a wide range of $n_{2d} \sim 2 - 6 \cdot 10^{13} \text{cm}^{-2}$. We also show that
6 the crossing of the second sub-band Q₂ occurs after a finite T_c is observed, while a full population
7 of both spin-orbit-split sub-bands (Fig.1d) in the Q/Q' valleys is required to reach the maximum
8 T_c . These results highlight how SC can be enhanced in MoS₂ by optimizing the connectivity of
9 its Fermi Surface (FS), i.e. by adding extra FSs in different BZ regions to provide coupling to
10 further phonon branches.⁴⁹ Since the evolution of the band structure of MoS₂ with field-effect
11 doping is analogous to that of other semiconducting TMDs,^{16,19,37,39,48} a similar mechanism is
12 likely associated with the emergence of SC in TMDs in general. Thus, optimization of the FS
13 connectivity can be a viable strategy in the search of new superconductors.

14
15 We study flakes with N=4-10, as Refs. 4,16,19 predicted that flakes with $N \geq 4$ are represen-
16 tative of the bulk electronic structure, and Ref. 33 experimentally observed that both T_c and the
17 critical magnetic field H_{c2} in 4L flakes are similar to those of 6L and bulk flakes. Our devices are
18 thus comparable with those in literature.^{26,33-35,50} We do not consider 1L flakes as they exhibit a
19 lower T_c and their mobility is suppressed due to disorder.^{33,50}

20
21 FL-MoS₂ flakes are prepared by micro-mechanical cleavage⁵¹ of 2H-MoS₂ crystals from SPI
22 Supplies. The 2H phase is selected to match that in previous reports of gate-induced SC.^{26,33} Low
23 resistivity ($< 0.005 \Omega \cdot \text{cm}$) Si coated with a thermal oxide SiO₂ is chosen as a substrate. We tested
24 both 90 or 285nm SiO₂ obtaining identical SC results. Thus, 90nm SiO₂ is used to minimize
25 the back gate voltage V_{BG} ($-30\text{V} < V_{BG} < 30\text{V}$), while 285nm is used to minimize leakage currents
26 through the back gate I_{BG} . Both SiO₂ thicknesses provide optical contrast at visible wavelengths.⁵²
27 A combination of optical contrast, Raman spectroscopy and atomic force microscopy (AFM) is
28 used to select the flakes and determine N.

29
30 Electrodes are then defined by patterning the contacts area by e-beam lithography, followed
31 by Ti:10nm/Au:50nm evaporation and lift-off. Ti is used as an adhesion layer,⁵³ while the thicker
32 Au layer provides the electrical contact. Flakes with irregular shapes are further patterned in

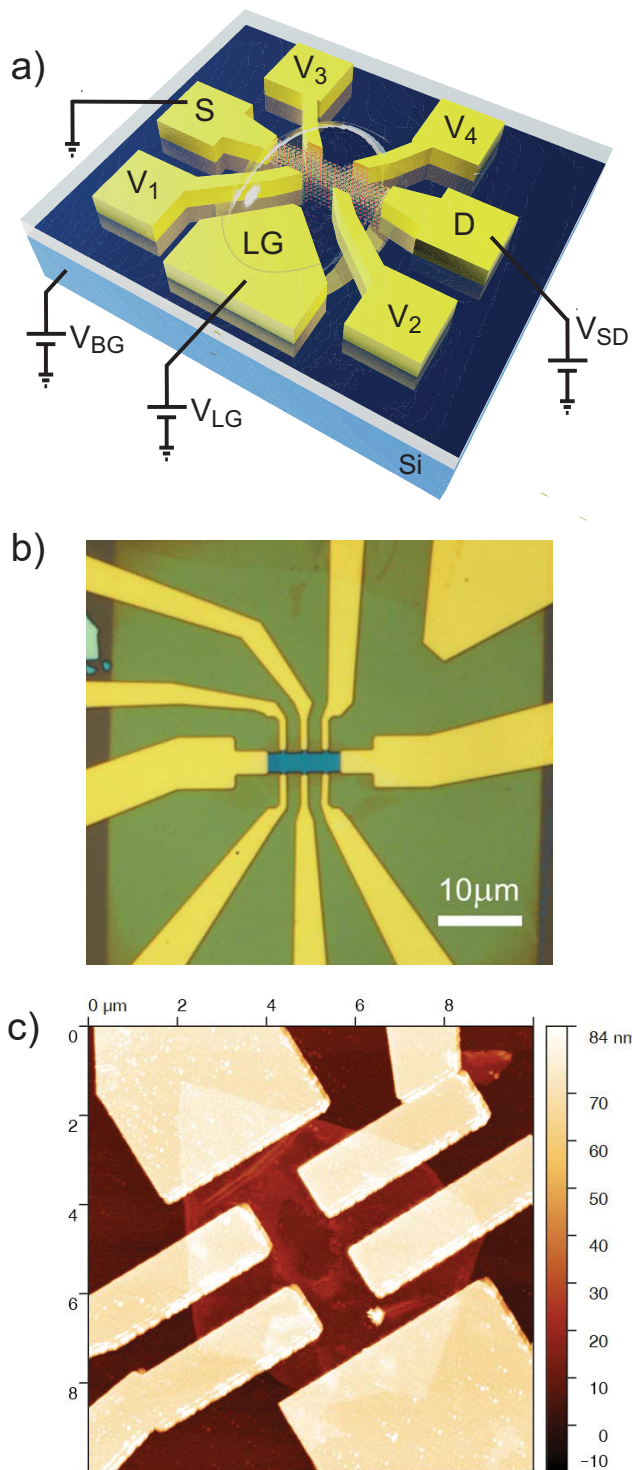


Figure 2: a) Hall bar FL-MoS₂ flake with voltage probes (V_i), source (S), drain (D) and liquid-gate (LG) electrodes. A ionic liquid droplet covers the flake and part of the LG electrode. The sample is biased with a source-drain voltage (V_{SD}) and dual gate control is enabled by a voltage applied on the liquid gate (V_{LG}) and on the solid back gate (V_{BG}). b) Optical image of Hall bar with six voltage probes. The LG electrode is on the upper-right corner. c) AFM scan of the MoS₂ Hall bar after ionic liquid removal.

the shape of Hall bars by using polymethyl methacrylate (PMMA) as a mask and removing the unprotected MoS₂ with reactive ion etching (RIE) in a 150mTorr atmosphere of CF₄:O₂=5:1, as shown in Figs.2a,b. A droplet of 1-Butyl-1-methylpiperidinium bis(trifluoromethylsulfonyl)imide (BMPPD-TFSI) is used to cover the FL-MoS₂ surface and part of the side electrode for liquid gate operation (LG), as sketched in Fig.2a.

AFM analysis is performed with a Bruker Dimension Icon in tapping mode. The scan in Fig.2c is done after the low-T experiments and removal of the ionic liquid, and confirms that the FL-MoS₂ sample does not show topographic damage after the measurement cycle.

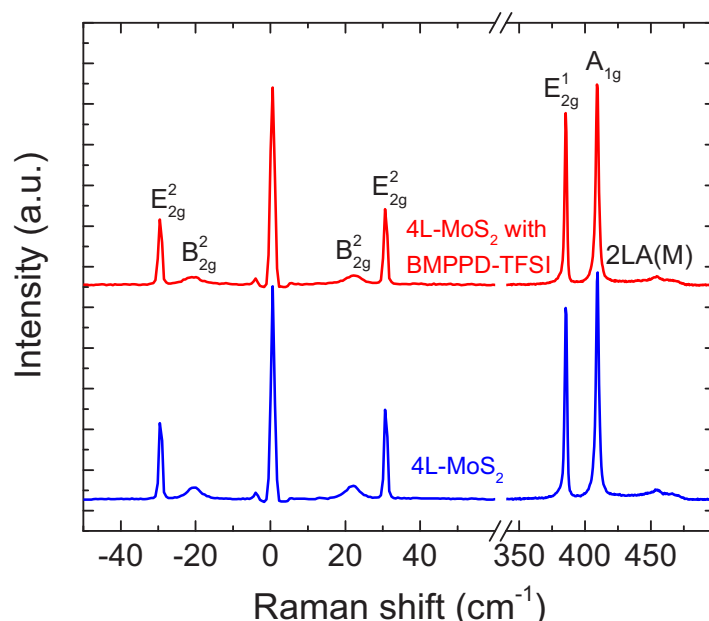


Figure 3: Representative Raman spectra at 514nm of a 4L-MoS₂ flake before (blue) and after (red) device fabrication, deposition of the ionic liquid droplet and low-T transport measurements.

We use Raman spectroscopy to characterize the devices both before and after fabrication and BMPPD-TFSI deposition. Raman measurements are performed with a Horiba LabRAM Evolution at 514nm, with a 1800grooves/mm grating and a spectral resolution $\sim 0.45\text{cm}^{-1}$. The power is kept below $300\mu\text{W}$ to avoid any damage. A representative Raman spectrum of 4L-MoS₂ is shown in Fig.3 (blue curve). The peak at $\sim 455\text{cm}^{-1}$ is due to a second-order longitudinal acoustic mode at the M point.⁵⁴ The E_{2g}^1 peak at $\sim 385\text{cm}^{-1}$ and the A_{1g} at $\sim 409\text{cm}^{-1}$ correspond to in-plane and out-of plane vibrations of Mo and S atoms.^{55,56} Their difference, $\text{Pos}(E_{2g}^1) - \text{Pos}(A_{1g})$, is often

used to monitor N .⁵⁷ However, for $N \geq 4$, the variation in $\text{Pos}(E_{2g}^1) - \text{Pos}(A_{1g})$ between N and $N+1$ approaches the instrument resolution⁵⁷ and this method is no longer reliable. Thus, we use the low frequency modes ($< 100\text{cm}^{-1}$) to monitor N .^{58,59} The shear (C) and layer breathing modes (LBM) are due to the relative motions of the atomic planes, either perpendicular or parallel to their normal.⁵⁸ $\text{Pos}(C)$ and $\text{Pos}(LBM)$ change with N as:^{58,59}

$$\text{Pos}(C)_N = \frac{1}{\sqrt{2\pi c}} \sqrt{\frac{\alpha_{\parallel}}{\mu_m}} \sqrt{1 + \cos\left(\frac{\pi}{N}\right)} \quad (1)$$

$$\text{Pos}(LBM)_N = \frac{1}{\sqrt{2\pi c}} \sqrt{\frac{\alpha_{\perp}}{\mu_m}} \sqrt{1 - \cos\left(\frac{\pi}{N}\right)} \quad (2)$$

where $\alpha_{\parallel} \sim 2.82 \cdot 10^{19} \text{N/m}^3$ and $\alpha_{\perp} \sim 8.90 \cdot 10^{19} \text{N/m}^3$ are spring constants for C and LBM modes, respectively, c is the speed of light in vacuum, $\mu_m \sim 3 \cdot 10^{-6} \text{Kg/m}^2$ is the 1L mass per unit area.^{58,59} Fig.3 shows a C mode at $\sim 30\text{cm}^{-1}$ and an LBM at $\sim 22\text{cm}^{-1}$. These correspond to $N=4$ using Eqs.1,2. Fig.3 also plots the Raman measurements after device fabrication, deposition of the ionic liquid, low-T measurements, V_{LG} removal and warm-up to room T (red curve). We still find $\text{Pos}(C) \sim 30\text{cm}^{-1}$ and $\text{Pos}(LBM) \sim 22\text{cm}^{-1}$, the same as those of the pristine flake, suggesting no damage nor residual doping.

Four-probe resistance and Hall measurements are then performed in the vacuum chambers of either a Cryomech pulse-tube cryocooler, $T_{min}=2.7\text{K}$, or a Lakeshore cryogenic probe-station, $T_{min}=8\text{K}$, equipped with a 2T superconducting magnet. A small ($\sim 1\mu\text{A}$) constant current is applied between S and D (Fig.2a) by using a two-channel Agilent B2912A source-measure unit (SMU). The longitudinal and transverse voltage drops are measured with an Agilent 34420 low-noise nanovoltmeter. Thermoelectrical and other offset voltages are eliminated by measuring each resistance value and inverting the source current in each measurement.⁶⁰ Gate biases are applied between the corresponding G and D with the same two-channel SMU (liquid gate) or a Keithley 2410 SMU (back gate). Samples are allowed to degas in vacuum ($< 10^{-5} \text{mbar}$) at room T for at least $\sim 1\text{h}$ before measurements, in order to remove residual water traces in the electrolyte.

We first characterize the T dependence of the sheet resistance, R_s , under the effect of the liquid

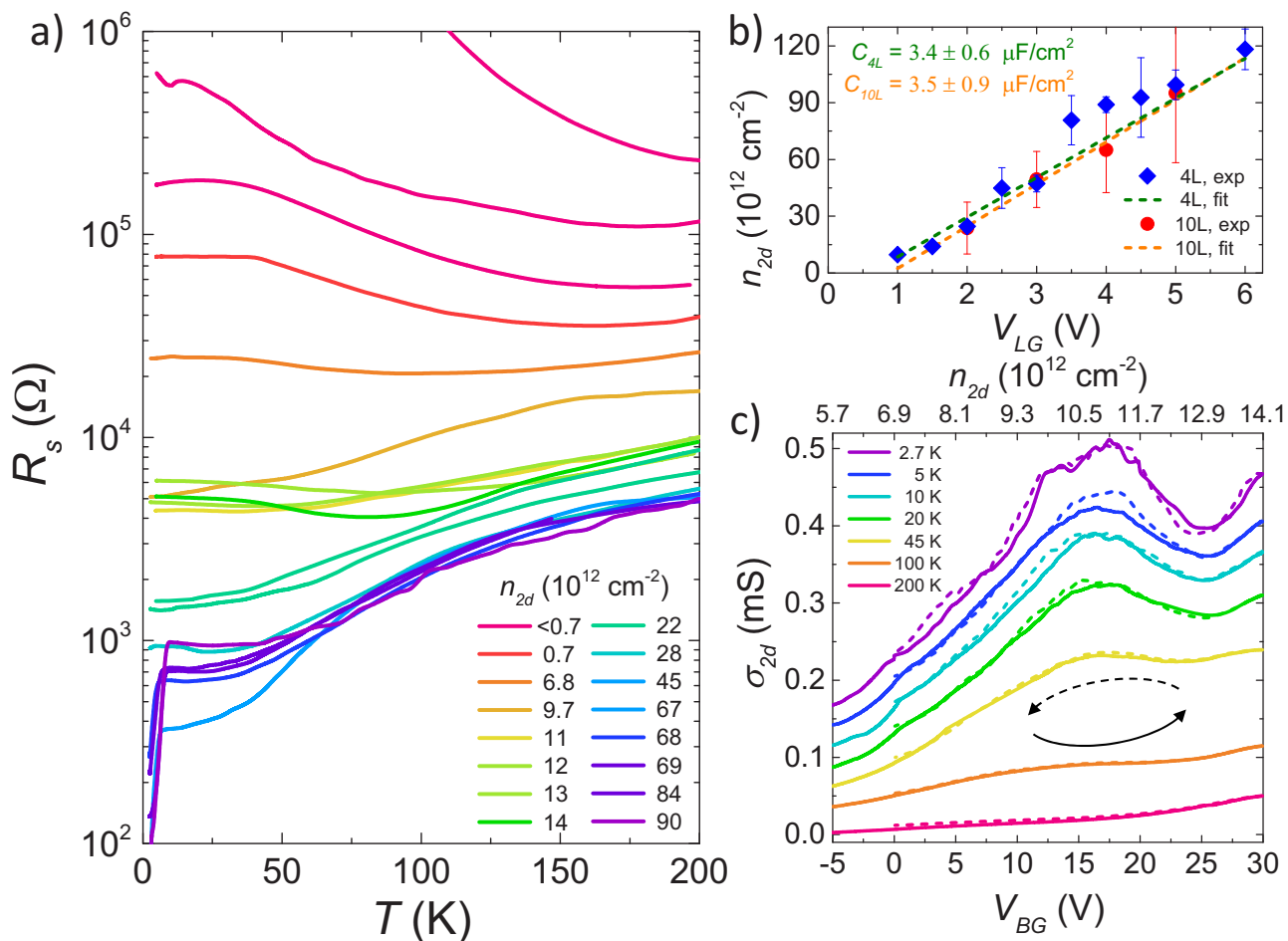


Figure 4: Transport of dual-gated 4L-MoS₂. a) R_s as a function of T for different n_{2d} . b) n_{2d} as function of V_{LG} as determined via Hall effect measurements, for $N=4, 10$. The liquid gate capacitances are obtained by a linear fit of the data. c) σ_{2d} as a function of V_{BG} at $V_{LG} = 0.9\text{V}$, for different T . Each curve is shifted by $3.333 \times 10^{-5}\text{S}$. The top scale shows the values of n_{2d} estimated from C_{ox} . Solid (dashed) curves are measured for increasing (decreasing) V_{BG} .

1
2
3 top gate. We apply the liquid gate voltage, V_{LG} , at 240K, where the electrolyte is still liquid, and
4 under high-vacuum ($< 10^{-5}$ mbar) to minimize unwanted electrochemical interactions and extend
5 the stability window of the ionic liquid.²⁴ After V_{LG} is applied, we allow the ion dynamics to settle
6 for ~ 10 min before cooling to a base $T=2.7$ K.
7
8
9

10
11 Fig.4a plots the T dependence of R_s measured in a four-probe configuration, for different V_{LG}
12 and induced carrier density n_{2d} . Our devices behave similarly to Ref. 26, undergoing first an
13 insulator-to-metal transition near $R_s \sim h/e^2$ at low $n_{2d} < 1 \cdot 10^{13} \text{cm}^{-2}$, followed by a metal-to-
14 superconductor transition at high $n_{2d} > 6 \cdot 10^{13} \text{cm}^{-2}$. The saturating behavior in the R_s vs T
15 curves in Fig.4a for $T \lesssim 50$ K, close to the insulator-to-metal transition, is typically observed in
16 systems at low n_{2d} characterized by a fluctuating electrostatic potential, such as that due to charged
17 impurities.⁶¹ This applies to ion-gated crystalline systems at low V_{LG} , since the doping is provided
18 by a low density of ions in close proximity to the active channel. These ions induce a perturbation
19 of the local electrostatic potential, locally inducing charge carriers, but are otherwise far apart.
20 The resulting potential landscape is thus inhomogeneous. This low-doping ($\lesssim 1 \times 10^{13} \text{cm}^{-2}$)
21 density inhomogeneity is a known issue in ion-gated crystalline systems, but becomes less and
22 less relevant at higher ionic densities.⁶² We employ Hall effect measurements to determine n_{2d}
23 as a function of V_{LG} (see Fig.4b), and, consequently, the liquid gate capacitance C_{LG} . C_{LG} for
24 the BMPPD-TFSI/MoS₂ interface ($\sim 3.4 \pm 0.6 \mu\text{F}/\text{cm}^2$) is of the same order of magnitude as for
25 DEME-TFSI/MoS₂ in Ref. 63 ($\sim 8.6 \pm 4.1 \mu\text{F}/\text{cm}^2$), where DEME-TFSI is the N,N-Diethyl-N-
26 methyl-N-(2-methoxyethyl)ammonium bis(trifluoromethanesulfonyl)imide ionic liquid.⁶³
27
28
29
30
31
32
33
34
35
36
37
38
39
40
41
42

43 Fig.4a shows that, while for $T \gtrsim 100$ K R_s is a monotonically decreasing function of n_{2d} , the
44 same does not hold for $T \lesssim 100$ K, where the various curves cross. In particular, the residual
45 R_s in the normal state R_s^0 (measured just above T_c when the flake is superconducting) varies
46 non-monotonically as a function of n_{2d} . This implies the existence of multiple local maxima
47 in the $R_s^0(n_{2d})$ curve. Consistently with the theoretical predictions of Ref. 19, we find two lo-
48 cal maxima. The first and more pronounced occurs when the flake is superconducting, i.e. for
49 $n_{2d} > 6 \cdot 10^{13} \text{cm}^{-2}$. This feature was also reported in Refs. 26,34, but not discussed. The second,
50
51
52
53
54
55
56
57
58
59
60

less pronounced kink, is observed for $1 \cdot 10^{13} \lesssim n_{2d} \lesssim 2 \cdot 10^{13} \text{cm}^{-2}$, not previously shown. Both kinks can be seen only for $T \lesssim 70\text{K}$ and they are smeared for $T \gtrsim 150\text{K}$.

The kink that emerges in the same range of n_{2d} as the superconducting dome extends across a wide range of V_{LG} ($3 \lesssim V_{LG} \lesssim 6\text{V}$) for $n_{2d} \gtrsim 6 \cdot 10^{13} \text{cm}^{-2}$, and can be accessed only by LG biasing, due to the small capacitance of the solid BG. This prevents a continuous characterization of its behavior, as n_{2d} induced by LG cannot be altered for $T \lesssim 220\text{K}$, as the ions are locked when the electrolyte is frozen. The kink that appears early in the metallic state, on the other hand, extends across a small range of n_{2d} ($1 \lesssim n_{2d} \lesssim 2 \cdot 10^{13} \text{cm}^{-2}$), and is ideally suited to be explored continuously by exploiting the dual-gate configuration.

We thus bias our samples in the low-density range of the metallic state ($n_{2d} \sim 7 \cdot 10^{12} \text{cm}^{-2}$) by applying $V_{LG} = 0.9\text{V}$, and cool the system to 2.7K . We then apply V_{BG} and fine-tune n_{2d} across the kink. We constantly monitor I_{BG} to avoid dielectric breakdown. Fig.4c plots σ_{2d} of a representative device subject to multiple V_{BG} sweeps, as n_{2d} is tuned across the kink. This reproduces well the behavior observed for low V_{LG} ($1 \lesssim n_{2d} \lesssim 2 \cdot 10^{13} \text{cm}^{-2}$). The hysteresis between increasing and decreasing V_{BG} is minimal. This kink is suppressed by increasing T, similar to LG gating.

V_{BG} provides us an independent tool to estimate n_{2d} : If V_{LG} is small enough ($V_{LG} \lesssim 1\text{V}$) so that conduction in the channel can be switched off by sufficiently large negative V_{BG} ($V_{BG} \lesssim -25\text{V}$), we can write $n_{2d} = C_{ox}/e \cdot (V_{BG} - V_{th})$. Here, $C_{ox} = \epsilon_{ox}/d_{ox}$ is the back gate oxide specific capacitance, $e = 1.602 \cdot 10^{-19}\text{C}$ is the elementary charge and V_{th} is the threshold voltage required to observe a finite conductivity in the device. We neglect the quantum capacitance C_q of MoS_2 , since $C_q \gtrsim 100\mu\text{F}/\text{cm}^2 \gg C_{ox}$.¹⁶ By using the dielectric constant of SiO_2 $\epsilon_{ox}=3.9$ ⁶⁴ and an oxide thickness $t_{ox} = 90\text{nm}$ (or $t_{ox} = 285\text{nm}$, depending on the experiment) we obtain the n_{2d} scale in the top axis of Fig.4c, in good agreement with the corresponding values in Fig.4a, estimated from the Hall effect measurements in Fig.4b.

The bandstructure of field-effect doped NL- MoS_2 depends on N ¹⁶ and strain.¹⁹ A fully relaxed N-layer flake, with $N \geq 3$, has been predicted to behave as follows:^{16,19} For small doping ($x \lesssim 0.05e^-/\text{unit cell}$, Figs.1b and 5a) only the two spin-orbit split sub-bands at K/K' are populated. At

intermediate doping ($0.05 \lesssim x \lesssim 0.1$ e⁻/unit cell, Figs.1c and 5b), E_F crosses the first spin-orbit split sub-band at Q/Q' (labeled Q_1). For large doping ($x \gtrsim 0.1$ e⁻/unit cell, Figs.1d and 5c) E_F crosses the second sub-band (Q_2) and both valleys become highly populated.¹⁶ Even larger doping ($x \gtrsim 0.35$ e⁻/unit cell) eventually shifts the K/K' valleys above E_F .¹⁶

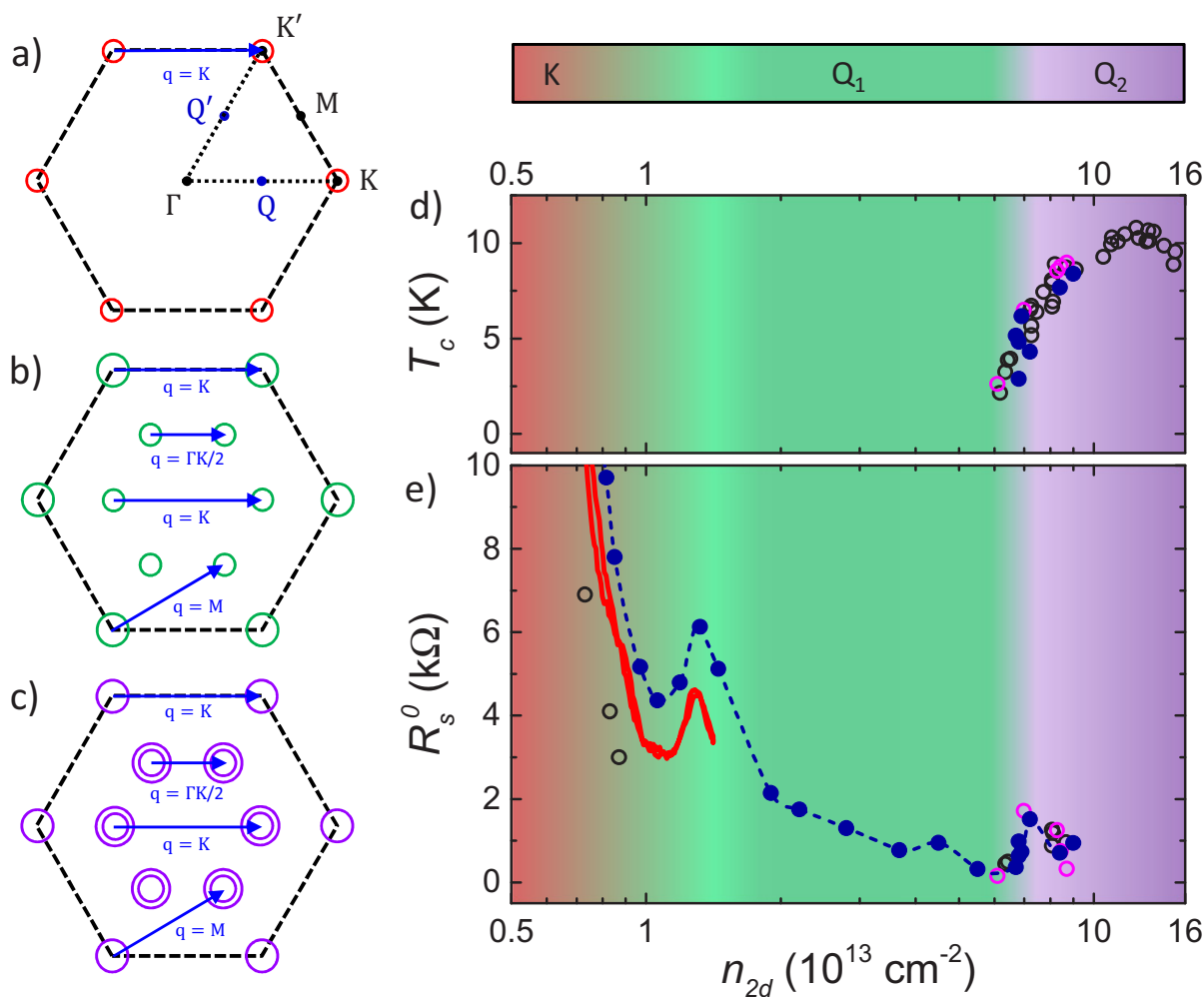


Figure 5: a-c) Fermi Surface of 3L-MoS₂ for the 3 doping values in Fig.1b-d. High symmetry points Γ , M, K, K', and points Q and Q' are shown. Blue arrows indicate representative phonon wave vectors that connect the various FSs. d) SC dome of liquid-gated MoS₂ as a function of n_{2d} . T_c is determined at 90% of the total transition. e) R_s^0 as a function of n_{2d} , for increasing V_{LG} (blue filled circles) and V_{BG} (solid red line). In d,e), filled circles are our data, black and magenta open circles are taken from Refs. 26,34. The background is color-coded to indicate the doping ranges highlighted in a-c).

When E_F crosses these high-energy sub-bands at Q/Q', sharp kinks are expected to appear in the transconductance of gated FL-MoS₂¹⁹ (see Fig.1e). These are reminiscent of a similar

behavior in liquid-gated FL graphene, where their appearance was linked to the opening of inter-band scattering channels upon the crossing of high-energy sub-bands.^{65–67} Even in the absence of energy-dependent scattering, Ref. 19 showed that σ_{2d} can be expressed as:

$$\sigma_{2d} = e^2 \tau \langle v_{\parallel}^2 \rangle N(E_F) \propto e^2 \langle v_{\parallel}^2 \rangle \quad (3)$$

where $\tau \propto N(E_F)^{-1}$ is the average scattering time, and $N(E_F)$ is the density of states (DOS) at E_F . This implies that σ_{2d} is proportional to the average of the squared in-plane velocity $\langle v_{\parallel}^2 \rangle$ over the FS.¹⁹ Since $\langle v_{\parallel}^2 \rangle$ linearly increases with n_{2d} and drops sharply as soon as a new band starts to get doped,¹⁹ the kinks in σ_{2d} (or, equivalently, R_s) at $T \lesssim 15\text{K}$ can be used to determine the onset of doping of the sub-bands in the Q/Q' valleys. At $T=0$, the kink is a sharp drop in σ_{2d} , emerging for the doping value at which E_F crosses the bottom of the next sub-band. This correspondence is lost due to thermal broadening for $T>0$, leading to a smoother variation in σ_{2d} . If T is sufficiently large the broadening smears out any signature of the kinks, Fig.4. Ref. 19 calculated that, at finite T , the conductivity kinks define a *doping range* where the sub-band crossing occurs (between R_s minimum and maximum, i.e. the *lower* and *upper* bounds of each kink sets the resolution of this approach). Each sub-band crossing starts after the R_s minimum at lower doping, then develops in correspondence of the inflection point, and is complete once the R_s maximum is reached.

We show evidence for this behavior in Fig.5, where we plot T_c (panel d) and R_s^0 (panel e) as a function of n_{2d} . The electric field is applied both in liquid-top-gate (filled dots and dashed line) and dual-gate (solid red line) configurations. For comparable values of n_{2d} , the liquid-gate geometry features larger R_s^0 than back-gated. This difference is due to increased disorder introduced when n_{2d} is modulated via ionic gating.^{66–70} Two kinks appear in the n_{2d} dependence of R_s : a low-doping one for $1.5 \cdot 10^{13} \lesssim n_{2d} \lesssim 2 \cdot 10^{13} \text{cm}^{-2}$, and a high-doping one for $7 \cdot 10^{13} \lesssim n_{2d} \lesssim 9 \cdot 10^{13} \text{cm}^{-2}$. The plot of the SC dome of gated MoS₂ on the same n_{2d} scale shows that the low-doping kink appears well before the SC onset, while the second appears immediately after, before the maximum T_c is reached.

These results can be interpreted as follows. When $n_{2d} \lesssim 1 \cdot 10^{13} \text{cm}^{-2}$, only the spin-orbit split sub-bands at K/K' are populated, and the FS is composed only by two pockets, Fig.5a. For n_{2d} between ~ 1.5 and $2 \cdot 10^{13} \text{cm}^{-2}$, E_F crosses the bottom of the Q_1 sub-band and two extra pockets appear in the FS at Q/Q',^{16,21} Fig.5b. The emergence of these pockets induces a Lifshitz transition, i.e. an abrupt change in the topology of the FS.⁷¹ Once Q_1 is populated and E_F is large enough ($n_{2d} \sim 6 \cdot 10^{13} \text{cm}^{-2}$), the system becomes superconducting.^{26,34} For slightly larger E_F ($7 \cdot 10^{13} \lesssim n_{2d} \lesssim 9 \cdot 10^{13} \text{cm}^{-2}$), E_F crosses the bottom of Q_2 resulting in a second Lifshitz transition, and other two pockets emerge in the FS at Q/Q',¹⁶ Fig.5c.

We note that the experimentally observed kinks are at different n_{2d} with respect to the theoretical ones for 3L-MoS₂.¹⁹ Ref. 19 predicted that for a 1.28% in-plane tensile strain, Q_1 and Q_2 should be crossed for $n_{2d} \sim 5 \cdot 10^{13}$ and $\sim 1 \cdot 10^{14}$. Since the positions of the sub-band crossings are strongly dependent on strain,¹⁹ we estimate the strain in our devices by monitoring the frequency of the E_{2g}^1 mode via Raman spectroscopy. Strain can arise due to a mismatch in the thermal expansion coefficients (TECs) of MoS₂,⁷² SiO₂ substrate⁷³ and Au electrodes.⁷⁴ Upon cooling, MoS₂, SiO₂ and Au would normally undergo a contraction. However the flake is also subject to a tensile strain due to TEC mismatch.⁷⁵ The strain, ϵ_{MoS_2} , due to the MoS₂-SiO₂ TEC mismatch is:

$$\epsilon_{MoS_2} = \int_T^{292K} [\alpha_{MoS_2}(T) - \alpha_{SiO_2}(T)] dT \quad (4)$$

whereas the strain, ϵ_{Au} , due to the Au contacts is:

$$\epsilon_{Au} = \int_T^{292K} [\alpha_{Au}(T) - \alpha_{SiO_2}(T)] dT \quad (5)$$

ϵ_{MoS_2} and ϵ_{Au} are $\sim 0.1\%$ and $\sim 0.3\%$ at $\sim 4\text{K}$, respectively.⁷⁵

Any FL-MoS₂ on SiO₂ will be subject to ϵ_{MoS_2} at low T. When the flake is contacted, an additional contribution is present due to ϵ_{Au} . This can be more reliably estimated performing T-dependent Raman scattering and comparing the spectra for contacted and un-contacted flakes.^{75,76} Figs.6a,b show how a T decrease results in the E_{2g}^1 mode shifting to higher frequencies for both

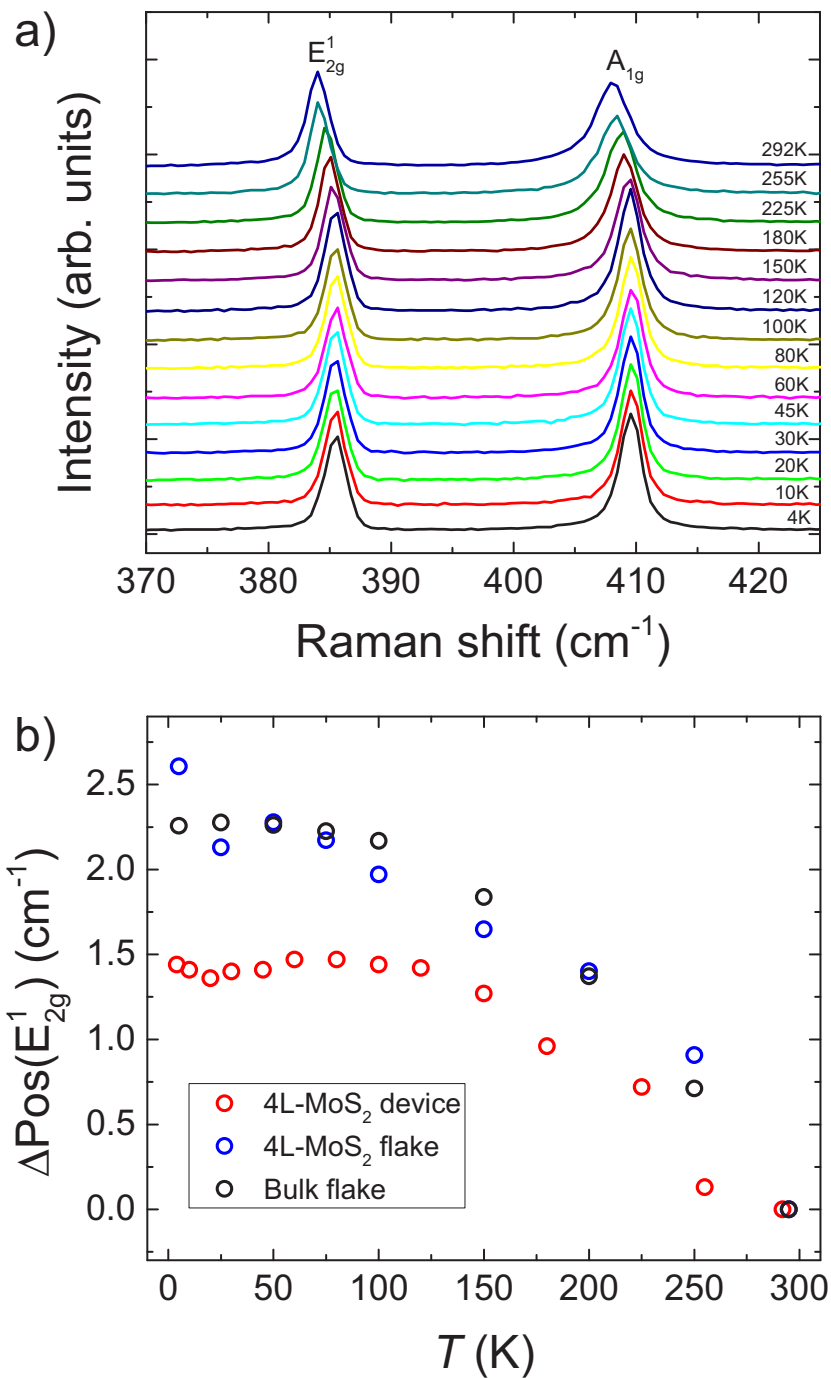


Figure 6: a) Raman spectra of the 4L-MoS₂ device in Fig.2c from 4 to 292K. b) Shift in the position of the E_{2g}^1 mode as a function of T for as-prepared bulk flake (black circles), a 4L-MoS₂ flake (blue circles), and a 4L-MoS₂ device with Au contacts (red circles).

1
2
3 as-prepared and contacted 4L-MoS₂, due to anharmonicity.⁷⁷ However, in the as-prepared 4L-
4 MoS₂, the up-shift is $\sim 1\text{cm}^{-1}$ larger with respect to the contacted one. This difference points to a
5 further tensile strain. Refs. 78,79 suggested that uniaxial tensile strain on 1L-MoS₂ induces a E_{2g}^1
6 softening and a splitting in two components: E_{2g}^{1+} and E_{2g}^{1-} .^{78,79} The shift rates for E_{2g}^{1+} and E_{2g}^{1-}
7 are from -0.9 to $-1.0\text{cm}^{-1}/\%$ and from -4.0 to $-4.5\text{cm}^{-1}/\%$, respectively.^{78,79} We do not observe
8 splitting, pointing towards a biaxial strain. As for Ref. 76, we calculate a shift rate of E_{2g}^1 for biaxial
9 strain from -7.2 to $-8.2\text{cm}^{-1}/\%$. The amount of tensile strain on the 4L-MoS₂ device can thus be
10 estimated. The E_{2g}^1 up-shift difference between contacted and as-prepared 4L-MoS₂, $\Delta\text{Pos}(E_{2g}^1)$,
11 at 4K is $\sim 1.0\text{cm}^{-1}$, corresponding to an additional $\sim 0.13\%$ biaxial tensile strain. Thus, assuming
12 a 0.1% strain for the as-prepared 4L-MoS₂ due to TEC mismatch with SiO₂, we estimate the total
13 strain in the contacted 4L-MoS₂ to be $\sim 0.23\%$ at $\sim 4\text{K}$.
14
15
16
17
18
19
20
21
22
23
24

25 Fig.7a shows that, for 0.23% tensile strain, the experimentally observed positions of the kinks
26 agree well with a linear extrapolation of the data of Ref. 19 to 4L-MoS₂ (representative of our
27 experiments) and for in-plane strain between 0% (bulk) and 1.28% (fully relaxed). These findings
28 indicate that, while the mechanism proposed in Ref. 21 qualitatively describes the general behavior
29 of gated FL-MoS₂, quantitative differences arise due to the spin-orbit split of the Q₁ and Q₂ sub-
30 bands. The main reason for the EPC (and, hence, T_c) increase is the same, i.e. the increase in the
31 number of phonon branches involved in the coupling when the high-energy valleys are populated.²¹
32 However, the finite spin-orbit-split between the sub-bands significantly alters the FS connectivity
33 upon increasing doping.¹⁶ If we consider the relevant phonon wave vectors ($q=\Gamma, K, M, \Gamma K/2$) for
34 1L- and FL-MoS₂,^{80,81} and only the K/K' valleys populated, then only phonons near Γ and K
35 can contribute to EPC.²¹ The former strongly couple e^- within the same valley,²¹ but cannot
36 contribute significantly due to the limited size of the Fermi sheets.²¹ The latter couple e^- across
37 different valleys,²¹ and provide a larger contribution,²¹ insufficient to induce SC. MoS₂ flakes are
38 metallic but not superconducting before the crossing of Q₁. When this crossing happens, the total
39 EPC increases due to the contribution of longitudinal phonon modes near K²¹ (coupling states
40 near two different Q or Q'), near $\Gamma K/2$ ²¹ (coupling states near Q to states near Q'), and near M²¹
41
42
43
44
45
46
47
48
49
50
51
52
53
54
55
56
57
58
59
60

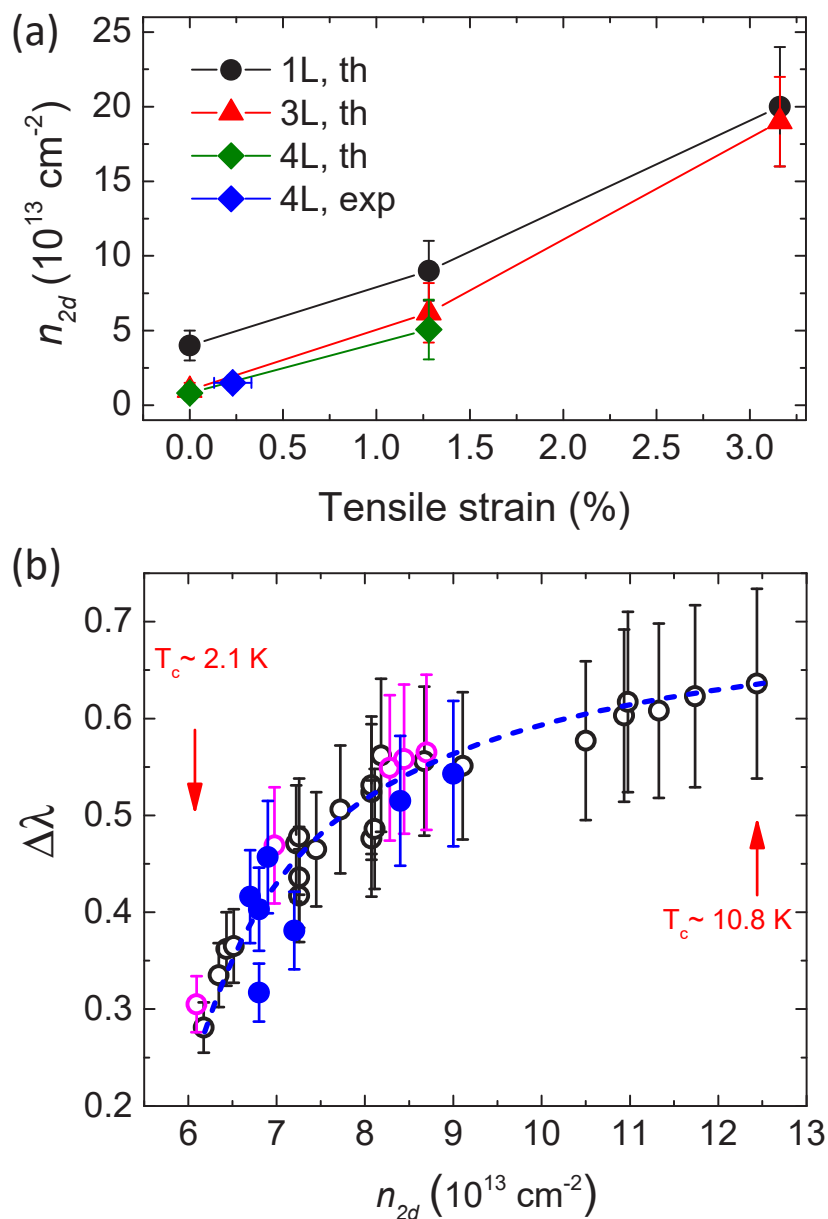


Figure 7: a) Surface carrier densities required to cross the Q_1 sub-band in FL-MoS₂ as a function of tensile strain. Theoretical values for 1L (black dots and line) and 3L (red triangle and line) from Ref. 19; values for 4L (green diamonds and line) are by linear extrapolation. Blue diamond is the present experiment. b) EPC enhancement due to the crossing of the Q_2 sub-band, $\Delta\lambda$, as a function of n_{2d} , assuming $\omega_{ln} = 230 \pm 30 \text{ K}$ and $\mu^* = 0.13$.²¹ Filled blue circles are our experiments. Black and magenta open circles from Refs. 26,34. The blue dashed line is a guide to the eye.

(coupling states near Q or Q' to states near K or K'). However, this first EPC increase associated with Q₁ is not sufficient to induce SC, as the SC transition is not observed until immediately before the crossing of the spin-orbit-split sub-band Q₂ and the second doping-induced Lifshitz transition. Additionally, the SC dome shows a maximum in the increase of T_c with doping (dT_c/dn_{2d}) across the Q₂ crossing, i.e. when a new FS emerges. Consistently, the subsequent reduction of T_c for $n_{2d} \geq 13 \cdot 10^{13} \text{cm}^{-2}$ can be associated with the FS shrinkage and disappearance at K/K',^{16,21} and might also be promoted by the formation of an incipient Charge Density Wave^{82,83} (characterized by periodic modulations of the carrier density coupled to a distortion of the lattice structure⁸⁴).

Since the evolution of the bandstructure with doping is similar in several semiconducting TMDs,^{16,19,37,39,48} this mechanism is likely not restricted to gated MoS₂. The T_c increase in correspondence to a Lifshitz transition is reminiscent of a similar behavior observed in CaFe₂As₂ under pressure,⁸⁵ suggesting this may be a general feature across different classes of materials.

We note that the maximum $T_c \sim 11\text{K}$ is reached at $n_{2d} \simeq 12 \cdot 10^{13} \text{cm}^{-2}$, as reported in Ref. 26. This is a doping level larger than any doping level which can be associated with the kink. Thus, the Q₂ sub-band must be highly populated when the maximum T_c is observed. We address this quantitatively with the Allen-Dynes formula,⁸⁶ which describes the dependence of T_c by a numerical approximation of the Eliashberg theory accurate for materials with a total $\lambda \lesssim 1.5$.⁸⁶

$$T_c(n_{2d}) = \frac{\omega_{ln}}{1.2} \exp \left\{ \frac{-1.04 [1 + \lambda(n_{2d})]}{\lambda(n_{2d}) - \mu^* [1 + 0.62\lambda(n_{2d})]} \right\} \quad (6)$$

where $\lambda(n_{2d})$ is the total EPC as a function of doping, ω_{ln} is the representative phonon frequency and μ^* is the Coulomb pseudo-potential. It is important to evaluate the increase in EPC between the non-superconducting region ($n_{2d} \lesssim 6 \times 10^{13} \text{cm}^{-2}$) and the superconducting one, i.e. the enhancement in λ due to the crossing of the sub-band at Q₂. $\Delta\lambda = \lambda(T_c) - \lambda(T_c = 0)$ indicates the EPC increase due to the appearance of e⁻ pockets at Q₂. By setting $\omega_{ln} = 230 \pm 30\text{K}$ and $\mu^* = 0.13$ (as for Ref. 21), and using Eq.6, we find that the limit of $\lambda(T_c)$ for $T_c \rightarrow 0$ is ~ 0.25 . The corresponding $\Delta\lambda$ vs. n_{2d} dependence is shown in Fig.7b. The crossing at Q₂ results in a

1
2
3 maximum $\Delta\lambda = 0.63 \pm 0.1$, with a maximum EPC enhancement of $350 \pm 40\%$ with respect to the
4 non-superconducting region. This indicates that the largest contribution to the total EPC, hence to
5 the maximum $T_c \sim 11\text{K}$, is associated with the population of the Q_2 sub-band. This is consistent
6 with the reports of a reduced $T_c \sim 2\text{K}$ in 1L-MoS₂,^{33,50} shown to be superconducting for smaller
7 $n_{2d} \sim 5.5 \cdot 10^{13}\text{cm}^{-2}$,⁵⁰ hence likely to populate Q_1 only. $n_{2d} \sim 5 \cdot 10^{13}\text{cm}^{-2}$ is also the doping
8 expected for the crossing of Q_1 in 1L-MoS₂ in presence of a low-T strain similar to that in our
9 4L-MoS₂ devices (see Fig.7a).

10
11 In summary, we exploited the large carrier density modulation provided by ionic gating to
12 explore sub-band population and multivalley transport in MoS₂ layers. We detected two kinks
13 in the conductivity, associated with the doping-induced crossing of the two sub-bands at Q/Q' .
14 By comparing the emergence of these kinks with the doping dependence of T_c , we showed how
15 superconductivity emerges in gated MoS₂ when the Q/Q' valleys are populated, while previous
16 works only considered the filling of K/K' . We highlighted the critical role of the population of the
17 second spin-orbit-split sub-band, Q_2 , (and the consequent increase of the FS available for EPC)
18 in the appearance of superconductivity and in the large enhancement of T_c and of EPC in the first
19 half of the superconducting dome. Our findings explain the doping dependence of the SC state at
20 the surface of gated FL-MoS₂, and provide a key insight for other semiconducting transition metal
21 dichalcogenides.
22
23
24
25
26
27
28
29
30
31
32
33
34
35
36
37
38
39
40

41 **Acknowledgments**

42 We thank M. Calandra for useful discussions. We acknowledge funding from EU Graphene Flag-
43 ship, ERC Grant Hetero2D, EPSRC Grant Nos. EP/509K01711X/1, EP/K017144/1, EP/N010345/1,
44 EP/M507799/ 5101, and EP/L016087/1 and the Joint Project for the Internationalization of Re-
45 search 2015 by Politecnico di Torino and Compagnia di San Paolo.
46
47
48
49
50

51 The authors declare no competing financial interests.
52
53
54
55
56
57
58
59
60

References

- (1) Ferrari, A. C.; Bonaccorso, F.; Fal'ko, V.; Novoselov, K. S.; Roche, S.; Bøggild, P.; Borini, S.; Koppens, F. H.; Palermo, V.; Pugno, N.; Garrido, José A.; Sordan, R.; Bianco, A.; Ballerini, L.; Prato, M.; Lidorikis, E.; Kivioja, J.; Marinelli, C.; Ryhänen; Morpurgo, A. F.; Coleman, J. N.; Nicolosi, V.; Colombo, L.; Fert, A.; Garcia-Hernandez, M.; Bachtold, A.; Schneider, G. F.; Guinea, F.; Dekker, C.; Barbone, M.; Sun, Z.; Galiotis, C.; Grigorenko, A. N.; Konstantatos, G.; Kis, A.; Katsnelson, M.; Vandersypen, L.; Loiseau, A.; Morandi, V.; Neumaier, D.; Treossi, E.; Pellegrini, V.; Polini, M.; Tredicucci, M.; Williams, G. M.; Hong, B. H.; Ahn, J.-H.; Kim, J. M.; Zirath, H.; van Wees, B. J.; van der Zant, H.; Occhipinti, L.; Di Matteo, A.; Kinloch, I. A.; Seyller, T.; Quesnel, E.; Feng, X.; Teo, K.; Rupesinghe, N.; Hakonen, P.; Neil, S. R. T.; Tannock, Q.; Löfwander, T.; Kinaret, J. Science and technology roadmap for graphene, related two-dimensional crystals, and hybrid systems. *Nanoscale* **2015**, *7*, 4598–4810
- (2) Wang, Q. H.; Kalantar-Zadeh, K.; Kis, A.; Coleman, J. N.; Strano, M. S. Electronics and optoelectronics of two-dimensional transition metal dichalcogenides. *Nature Nanotech.* **2012**, *7*, 699
- (3) Mak, K. F.; Lee, C.; Hone, J.; Shan, J.; Heinz, T. F. Atomically thin MoS₂: a new direct-gap semiconductor. *Phys. Rev. Lett.* **2010**, *105*, 136805
- (4) Splendiani, A.; Sun, L.; Zhang, Y.; Li, T.; Kim, J.; Chim, C.-Y.; Galli, G.; Wang, F. Emerging photoluminescence in monolayer MoS₂. *Nano Lett.* **2010**, *10*, 1271–1275
- (5) Mak, K. F.; Shan, J. Photonics and optoelectronics of 2D semiconductor transition metal dichalcogenides. *Nature Phot.* **2016**, *10*, 216
- (6) Podzorov, V.; Gershenson, M.; Kloc, C.; Zeis, R.; Bucher, E. High-mobility field-effect transistors based on transition metal dichalcogenides. *Appl. Phys. Lett.* **2004**, *84*, 3301–3303

- 1
2
3 (7) Radisavljevic, B.; Radenovic, A.; Brivio, J.; Giacometti, i. V.; Kis, A. Single-layer MoS₂
4 transistors. *Nature Nanotech.* **2011**, *6*, 147
5
6
7
8 (8) Fang, H.; Chuang, S.; Chang, T. C.; Takei, K.; Takahashi, T.; Javey, A. High-performance
9 single layered WSe₂ p-FETs with chemically doped contacts. *Nano Lett.* **2012**, *12*, 3788–
10 3792
11
12
13
14 (9) Gourmelon, E.; Lignier, O.; Hadouda, H.; Couturier, G.; Bernede, J.; Tedd, J.; Pouzet, J.;
15 Salardenne, J. MS₂ (M= W, Mo) photosensitive thin films for solar cells. *Solar Energy Ma-*
16 *terials and Solar Cells* **1997**, *46*, 115–121
17
18
19
20 (10) Lee, H. S.; Min, S.-W.; Chang, Y.-G.; Park, M. K.; Nam, T.; Kim, H.; Kim, J. H.; Ryu, S.;
21 Im, S. MoS₂ nanosheet phototransistors with thickness-modulated optical energy gap. *Nano*
22 *Lett.* **2012**, *12*, 3695–3700
23
24
25
26
27 (11) Yin, Z.; Li, H.; Li, H.; Jiang, L.; Shi, Y.; Sun, Y.; Lu, G.; Zhang, Q.; Chen, X.; Zhang, H.
28 Single-layer MoS₂ phototransistors. *ACS Nano* **2011**, *6*, 74–80
29
30
31
32 (12) Koppens, F.; Mueller, T.; Avouris, P.; Ferrari, A.; Vitiello, M.; Polini, M. Photodetectors
33 based on graphene, other two-dimensional materials and hybrid systems. *Nature Nanotech.*
34 **2014**, *9*, 780
35
36
37
38 (13) Sun, Z.; Martinez, A.; Wang, F. Optical modulators with 2D layered materials. *Nature Phot.*
39 **2016**, *10*, 227
40
41
42
43 (14) Carladous, A.; Coratger, R.; Ajustron, F.; Seine, G.; Péchou, R.; Beauvillain, J. Light emis-
44 sion from spectral analysis of Au/MoS₂ nanocontacts stimulated by scanning tunneling mi-
45 croscopy. *Phys. Rev. B* **2002**, *66*, 045401
46
47
48
49 (15) Sundaram, R.; Engel, M.; Lombardo, A.; Krupke, R.; Ferrari, A.; Avouris, P.; Steiner, M.
50 Electroluminescence in single layer MoS₂. *Nano Lett.* **2013**, *13*, 1416–1421
51
52
53
54
55
56
57
58
59
60

- 1
2
3
4 (16) Brumme, T.; Calandra, M.; Mauri, F. First-principles theory of field-effect doping in
5 transition-metal dichalcogenides: Structural properties, electronic structure, Hall coefficient,
6 and electrical conductivity. *Phys. Rev. B* **2015**, *91*, 155436
7
8
9
10 (17) Giannozzi, P.; Andreussi, O.; Brumme, T.; Bunau, O.; Buongiorno Nardelli, M.; Calandra,
11 M.; Car, R.; Cavazzoni, C.; Ceresoli, D.; Cococcioni, M.; Colonna, N.; Carnimeo, I.; Dal
12 Corso, A.; de Gironcoli, S.; Delugas, P.; DiStasio Jr, R. A.; Ferretti, A.; Floris, A.; Fratesi,
13 G.; Fugallo, G.; Gebauer, R.; Gerstmann, U.; Giustino, F.; Gorni, T.; Jia, J.; Kawamura,
14 M.; Ko, H.-Y.; Kokalj, A.; Küçükbenli, E.; Lazzeri, M.; Marsili, M.; Marzari, N.; Mauri,
15 F.; Nguyen, N. L.; Nguyen, H.-V.; Otero-de-la-Roza, A.; Paulatto, L.; Poncé, S.; Rocca, D.;
16 Sabatini, R.; Santra, B.; Schlipf, M.; Seitsonen, A. P.; Smogunov, A.; Timrov, I.; Thonhauser,
17 T.; Umari, P.; Vast, N.; Wu, X.; Baroni, S. Advanced capabilities for materials modelling with
18 quantum espresso. *J. Phys.: Cond. Mat.* **2017** *29*, 465901
19
20
21
22
23
24
25
26
27
28
29 (18) Brumme, T.; Calandra, M.; Mauri, F. Electrochemical doping of few-layer ZrNCl from first
30 principles: Electronic and structural properties in field-effect configuration. *Phys. Rev. B* **2014**
31 *89*, 245406
32
33
34
35
36 (19) Brumme, T.; Calandra, M.; Mauri, F. Determination of scattering time and of valley oc-
37 cupation in transition-metal dichalcogenides doped by field effect. *Phys. Rev. B* **2016**, *93*,
38 081407(R)
39
40
41
42 (20) Cheiwchanchamnangij, T.; Lambrecht, W. R. Quasiparticle band structure calculation of
43 monolayer, bilayer, and bulk MoS₂. *Phys. Rev. B* **2012**, *85*, 205302
44
45
46
47 (21) Ge, Y.; Liu, A. Y. Phonon-mediated superconductivity in electron-doped single-layer MoS₂:
48 a first-principles prediction. *Phys. Rev. B* **2013**, *87*, 241408(R)
49
50
51
52 (22) Kadantsev, E. S.; Hawrylak, P. Electronic structure of a single MoS₂ monolayer. *Solid State*
53 *Comm.* **2012**, *152*, 909–913
54
55
56
57
58
59
60

- 1
2
3 (23) Fujimoto, T.; Awaga, K. Electric-double-layer field-effect transistors with ionic liquids. *Phys.*
4 *Chem. Chem. Phys.* **2013**, *15*, 8983–9006
5
6
7
8 (24) Ueno, K.; Shimotani, H.; Yuan, H.; Ye, J.; Kawasaki, M.; Iwasa, Y. Field-induced supercon-
9 ductivity in electric double layer transistors. *J. Phys. Soc. Japan* **2014**, *83*, 032001
10
11
12
13 (25) Saito, Y.; Nojima, T.; Iwasa, Y. Gate-induced superconductivity in two-dimensional atomic
14 crystals. *Superconductor Science Tech.* **2016**, *29*, 093001
15
16
17
18 (26) Ye, J.; Zhang, Y.; Akashi, R.; Bahramy, M.; Arita, R.; Iwasa, Y. Superconducting dome in a
19 gate-tuned band insulator. *Science* **2012**, *338*, 1193–1196
20
21
22
23 (27) Braga, D.; Gutiérrez Lezama, I.; Berger, H.; Morpurgo, A. F. Quantitative determination
24 of the band gap of WS₂ with ambipolar ionic liquid-gated transistors. *Nano Lett.* **2012**, *12*,
25 5218–5223
26
27
28
29 (28) Yu, Y.; Yang, F.; Lu, X. F.; Yan, Y. J.; Cho, Y.-H.; Ma, L.; Niu, X.; Kim, S.; Son, Y.-W.;
30 Feng, D.; Li, S.; Cheong, S.-W.; Chen, X. H.; Zhang, Y. Gate-tunable phase transitions in
31 thin flakes of 1T-TaS₂. *Nature Nanotech.* **2015**, *10*, 270
32
33
34
35
36 (29) Xi, X.; Berger, H.; Forró, L.; Shan, J.; Mak, K. F. Gate Tuning of Electronic Phase Transitions
37 in Two-Dimensional NbSe₂. *Phys. Rev. Lett.* **2016**, *117*, 106801
38
39
40
41 (30) Chakraborty, B.; Bera, A.; Muthu, D.; Bhowmick, S.; Waghmare, U. V.; Sood, A. Symmetry-
42 dependent phonon renormalization in monolayer MoS₂ transistor. *Phys. Rev. B* **2012**, *85*,
43 161403
44
45
46
47
48 (31) Das, A.; Pisana, S.; Chakraborty, B.; Piscanec, S.; Saha, S.; Waghmare, U.; Novoselov,
49 K.; Krishnamurthy, H.; Geim, A.; Ferrari, A.; Sood, A. K. Monitoring dopants by Raman
50 scattering in an electrochemically top-gated graphene transistor. *Nature Nanotech.* **2008**, *3*,
51 210
52
53
54
55
56
57
58
59
60

- 1
2
3 (32) Das, A.; Chakraborty, B.; Piscanec, S.; Pisana, S.; Sood, A.; Ferrari, A. Phonon renormaliza-
4 tion in doped bilayer graphene. *Phys. Rev. B* **2009**, *79*, 155417
5
6
7
8 (33) Costanzo, D.; Jo, S.; Berger, H.; Morpurgo, A. F. Gate-induced superconductivity in atomi-
9 cally thin MoS₂ crystals. *Nature Nanotech.* **2016**, *11*, 339
10
11
12 (34) Lu, J.; Zheliuk, O.; Leermakers, I.; Yuan, N. F.; Zeitler, U.; Law, K. T.; Ye, J. Evidence for
13 two-dimensional Ising superconductivity in gated MoS₂. *Science* **2015**, *350*, 1353–1357
14
15
16
17 (35) Saito, Y.; Nakamura, Y.; Bahramy, M. S.; Kohama, Y.; Ye, J.; Kasahara, Y.; Nakagawa, Y.;
18 Onga, M.; Tokunaga, M.; Nojima, T.; Yanase, Y.; Iwasa, Y. Superconductivity protected by
19 spin-valley locking in ion-gated MoS₂. *Nature Phys.* **2016**, *12*, 144–149
20
21
22
23
24 (36) Chen, Q.; Lu, J.; Liang, L.; Zheliuk, O.; Ali, A.; Sheng, P.; Ye, J. Inducing and Manipulating
25 Heteroelectronic States in a Single MoS₂ Thin Flake. *Phys. Rev. Lett.* **2017**, *119*, 147002
26
27
28
29 (37) Wu, Z.; Xu, S.; Lu, H.; Khamoshi, A.; Liu, G.-B.; Han, T.; Wu, Y.; Lin, J.; Long, G.;
30 He, Y.; Cai, Y.; Yao, Y.; Zhang, F.; Wang, N. Even–odd layer-dependent magnetotransport
31 of high-mobility Q-valley electrons in transition metal disulfides. *Nature Commun.* **2016**, *7*,
32 12955
33
34
35
36
37 (38) Roldán, R.; Cappelluti, E.; Guinea, F. Interactions and superconductivity in heavily doped
38 MoS₂. *Phys. Rev. B* **2013**, *88*, 054515
39
40
41
42 (39) Das, T.; Dolui, K. Superconducting dome in MoS₂ and TiSe₂ generated by quasiparticle-
43 phonon coupling. *Phys. Rev. B* **2015**, *91*, 094510
44
45
46
47 (40) Kormányos, A.; Zólyomi, V.; Drummond, N. D.; Rakyta, P.; Burkard, G.; Fal’ko, V. I. Mono-
48 layer MoS₂: trigonal warping, the Γ valley, and spin-orbit coupling effects. *Phys. Rev. B*
49 **2013**, *88*, 045416
50
51
52
53 (41) Yuan, N. F.; Mak, K. F.; Law, K. Possible topological superconducting phases of MoS₂. *Phys.*
54 *Rev. Lett.* **2014**, *113*, 097001
55
56
57
58
59
60

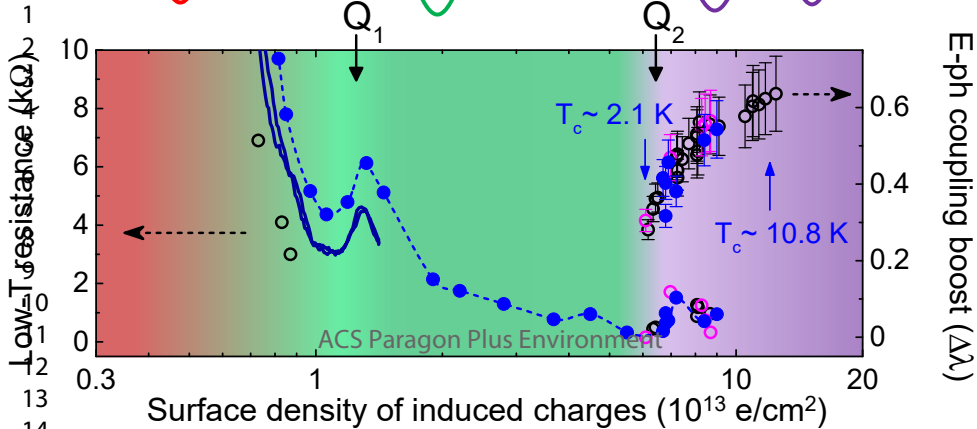
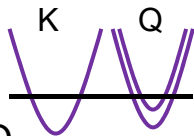
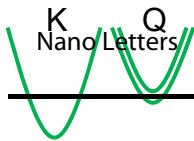
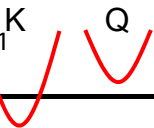
- 1
2
3 (42) Costanzo, D.; Zhang, H.; Reddy, B. A.; Berger, H.; Morpurgo, A. F. Tunnelling spectroscopy
4 of gate-induced superconductivity in MoS₂. *Nature Nanotech.* **2018** DOI:10.1038/s41565-
5 018-0122-2
6
7
8
9
10 (43) Hsu, Y.-T.; Vaezi, A.; Fischer, M. H.; Kim, E.-A. Topological superconductivity in monolayer
11 transition metal dichalcogenides. *Nature Comm.* **2017**, 8, 14985
12
13
14 (44) Nakamura, Y.; Yanase, Y. Odd-parity superconductivity in bilayer transition metal dichalco-
15 genides. *Phys. Rev. B* **2017**, 96, 054501
16
17
18
19 (45) Lu, J. M.; Zheliuk, O.; Chen, Q.; Leermakers, I.; Hussey, N. E.; Zeitler, U.; Ye, J. T. Full
20 superconducting dome of strong Ising protection in gated monolayer WS₂. *PNAS* **2018** 115,
21 3551
22
23
24
25
26 (46) de la Barrera, S. C.; Sinko, M. R.; Gopalan, D. P.; Sivadas, N.; Seyler, K. L.; Watanabe,
27 K.; Taniguchi, T.; Tsen, A. W.; Xu, X.; Xiao, D.; Hunt, B. M. Tuning Ising superconductiv-
28 ity with layer and spin-orbit coupling in two-dimensional transition-metal dichalcogenides.
29 *Nature Comm.* **2018** 9, 1427
30
31
32
33
34 (47) Cui, X.; Lee, G.-H.; Kim, Y. D.; Arefe, G.; Huang, P. Y.; Lee, C.-H.; Chenet, D. A.; Zhang,
35 X.; Wang, L.; Ye, F.; Pizzocchero, F.; Jessen, B. S.; Watanabe, K.; Taniguchi, T.; Muller, D.
36 A.; Low, T.; Kim, P.; Hone, J. Multi-terminal transport measurements of MoS₂ using a van
37 der Waals heterostructure device platform. *Nature Nanotech.* **2015**, 10, 534
38
39
40
41
42
43 (48) Kang, M.; Kim, B.; Ryu, S. H.; Jung, S. W.; Kim, J.; Moreschini, L.; Jozwiak, C.; Rotenberg,
44 E.; Bostwick, A.; Kim, K. S. Universal mechanism of band-gap engineering in transition-
45 metal dichalcogenides. *Nano Lett.* **2017**, 17, 1610-1615
46
47
48
49
50 (49) Pickett, W. E. *Emergent Phenomena in Correlated Matter*; Forschungszentrum Jülich GmbH
51 and Institute for Advanced Simulations: Jülich, Germany, 2013
52
53
54
55
56
57
58
59
60

- 1
2
3 (50) Fu, Y.; Liu, E.; Yuan, H.; Tang, P.; Lian, B.; Xu, G.; Zeng, J.; Chen, Z.; Wang, Y.; Zhou, W.;
4 Xu, K.; Gao, A.; Pan, C.; Wang, M.; Wang, B.; Zhang, S.-C.; Hwang, H. Y.; Miao, F. Gated
5 tuned superconductivity and phonon softening in monolayer and bilayer MoS₂. *npj Quantum*
6 *Materials* **2017**, *2*, 52
7
8
9
10
11
12 (51) Novoselov, K.; Jiang, D.; Schedin, F.; Booth, T.; Khotkevich, V.; Morozov, S.; Geim, A.
13 Two-dimensional atomic crystals. *PNAS* **2005**, *102*, 10451–10453
14
15
16
17 (52) Casiraghi, C.; Hartschuh, A.; Lidorikis, E.; Qian, H.; Harutyunyan, H.; Gokus, T.; Novoselov,
18 K.; Ferrari, A. Rayleigh imaging of graphene and graphene layers. *Nano Lett.* **2007**, *7*, 2711–
19 2717
20
21
22
23 (53) Kutz, M. *Handbook of Materials Selection*; John Wiley & Sons, 2002
24
25
26 (54) Stacy, A.; Hodul, D. Raman spectra of IVB and VIB transition metal disulfides using laser
27 energies near the absorption edges. *J. Phys. Chem. Sol.* **1985**, *46*, 405–409
28
29
30
31 (55) Verble, J.; Wieting, T. Lattice Mode Degeneracy in MoS₂ and Other Layer Compounds. *Phys.*
32 *Rev. Lett.* **1970**, *25*, 362
33
34
35
36 (56) Wieting, T.; Verble, J. Infrared and Raman Studies of Long-Wavelength Optical Phonons in
37 Hexagonal MoS₂. *Phys. Rev. B* **1971**, *3*, 4286
38
39
40
41 (57) Lee, C.; Yan, H.; Brus, L. E.; Heinz, T. F.; Hone, J.; Ryu, S. Anomalous lattice vibrations of
42 single-and few-layer MoS₂. *ACS Nano* **2010**, *4*, 2695-2700
43
44
45 (58) Zhang, X.; Han, W.; Wu, J.; Milana, S.; Lu, Y.; Li, Q.; Ferrari, A.; Tan, P. Raman spec-
46 troscopy of shear and layer breathing modes in multilayer MoS₂. *Phys. Rev. B* **2013**, *87*,
47 115413
48
49
50
51 (59) Tan, P.; Han, W.; Zhao, W.; Wu, Z.; Chang, K.; Wang, H.; Wang, Y.; Bonini, N.; Marzari, N.;
52 Pugno, N.; Savini, G.; Lombardo, A.; Ferrari, A. C. The shear mode of multilayer graphene.
53 *Nature Mater.* **2012**, *11*, 294
54
55
56
57
58
59
60

- 1
2
3 (60) Daghero, D.; Paolucci, F.; Sola, A.; Tortello, M.; Ummarino, G.; Agosto, M.; Gonnelli, R.;
4 Nair, J. R.; Gerbaldi, C. Large conductance modulation of gold thin films by huge charge
5 injection via electrochemical gating. *Phys. Rev. Lett.* **2012**, *108*, 066807
6
7
8
9
10 (61) Zabrodskii, A. G; Zinoveva, K. N. Low-temperature conductivity and metal-insulator transi-
11 tion in compensate n-Ge. *J. Exp. Theor. Phys.* **1984**, *59*, 425
12
13
14 (62) Ren, Y.; Yuan, H.; Wu, X.; Chen, Z.; Iwasa, Y.; Cui, Y.; Hwang, H. Y.; Lai, K. Direct Imaging
15 of Nanoscale Conductance Evolution in Ion-Gel-Gated Oxide Transistors. *Nano Lett.* **2015**
16 *15*, 4730
17
18
19
20
21 (63) Shi, W.; Ye, J.; Zhang, Y.; Suzuki, R.; Yoshida, M.; Miyazaki, J.; Inoue, N.; Saito, Y.;
22 Iwasa, Y. Superconductivity series in transition metal dichalcogenides by ionic gating. *Sci.*
23 *Rep.* **2015**, *5*, 12534
24
25
26
27
28 (64) El-Kareh, B. *Fundamentals of Semiconductor Processing Technologies*; Kluwer Academic
29 Publishers, 1995
30
31
32
33 (65) Ye, J.; Craciun, M. F.; Koshino, M.; Russo, S.; Inoue, S.; Yuan, H.; Shimotani, H.; Morpurgo,
34 A. F.; Iwasa, Y. Accessing the transport properties of graphene and its multilayers at high
35 carrier density. *PNAS* **2011**, *108*, 13002–13006
36
37
38
39
40 (66) Gonnelli, R.; Piatti, E.; Sola, A.; Tortello, M.; Dolcini, F.; Galasso, S.; Nair, J. R.; Gerbaldi,
41 C.; Cappelluti, E.; Bruna, M.; Ferrari, A. Weak localization in electric-double-layer gated
42 few-layer graphene. *2D Mater.* **2017**, *4*, 035006
43
44
45
46
47 (67) Piatti, E.; Galasso, S.; Tortello, M.; Nair, J. R.; Gerbaldi, C.; Bruna, M.; Borini, S.; Daghero,
48 D.; Gonnelli, R. Carrier mobility and scattering lifetime in electric double-layer gated few-
49 layer graphene. *Appl. Surf. Sci.* **2017**, *395*, 37–41
50
51
52
53 (68) Piatti, E.; Chen, Q.; Ye, J. Strong dopant dependence of electric transport in ion-gated MoS₂.
54 *Appl. Phys. Lett.* **2017**, *111*, 013106
55
56
57
58
59
60

- 1
2
3 (69) Gallagher, P.; Lee, M.; Petach, T. A.; Stanwyck, S. W.; Williams, J. R.; Watanabe, K.;
4 Taniguchi, T.; Goldhaber-Gordon, D. A high-mobility electronic system at an electrolyte-
5 gated oxide surface. *Nature Comm.* **2015**, *6*, 6437
6
7
8
9
10 (70) Ovchinnikov, D.; Gargiulo, F.; Allain, A.; Pasquier, D. J.; Dumcenco, D.; Ho, C.-H.; Yazyev,
11 O. V.; Kis, A. Disorder engineering and conductivity dome in ReS₂ with electrolyte gating.
12 *Nature Comm.* **2016**, *7*, 12391
13
14
15
16
17 (71) Lifshitz, I. Anomalies of electron characteristics of a metal in the high pressure region. *Sov.*
18 *Phys. JETP* **1960**, *11*, 1130–1135
19
20
21
22 (72) Gan, C. K.; Liu, Y. Y. F. Direct calculation of the linear thermal expansion coefficients of
23 MoS₂ via symmetry-preserving deformations. *Phys. Rev. B* **2016**, *94*, 134303
24
25
26
27 (73) *Standard Reference Material 739 Certificate*; National Institute of Standards and Technology:
28 Gaithersburg, MD, 1991
29
30
31 (74) Nix, F.; MacNair, D. The thermal expansion of pure metals: copper, gold, aluminum, nickel,
32 and iron. *Phys. Rev.* **1941**, *60*, 597
33
34
35
36 (75) Yoon, D.; Son, Y.-W.; Cheong, H. Negative thermal expansion coefficient of graphene mea-
37 sured by Raman spectroscopy. *Nano Lett.* **2011**, *11*, 3227–3231
38
39
40
41 (76) Mohiuddin, T.; Lombardo, A.; Nair, R.; Bonetti, A.; Savini, G.; Jalil, R.; Bonini, N.; Basko,
42 D.; Galiotis, C.; Marzari, N.; Pugno, N.; Savini, G.; Lombardo, A.; Ferrari, A. C. Uniaxial
43 strain in graphene by Raman spectroscopy: G peak splitting, Grüneisen parameters, and
44 sample orientation. *Phys. Rev. B* **2009**, *79*, 205433
45
46
47
48
49
50 (77) Klemens, P. Anharmonic decay of optical phonons. *Phys. Rev.* **1966**, *148*, 845
51
52
53 (78) Lee, J.-U.; Woo, S.; Park, J.; Park, H.; Son, Y.-W.; Cheong, H. Strain-shear coupling in
54 bilayer MoS₂. *Nature Comm.* **2017**, *8*, 1370
55
56
57
58
59
60

- 1
2
3 (79) Conley, H. J.; Wang, B.; Ziegler, J. I.; Haglund Jr, R. F.; Pantelides, S. T.; Bolotin, K. I.
4 Bandgap engineering of strained monolayer and bilayer MoS₂. *Nano Lett.* **2013**, *13*, 3626–
5 3630
6
7
8
9
10 (80) Molina-Sanchez, A.; Wirtz, L. Phonons in single-layer and few-layer MoS₂ and WS₂. *Phys.*
11 *Rev. B* **2011**, *84*, 155413
12
13
14 (81) Ataca, C.; Topsakal, M.; Akturk, E.; Ciraci, S. A comparative study of lattice dynamics of
15 three-and two-dimensional MoS₂. *J. Phys. Chem. C* **2011**, *115*, 16354–16361
16
17
18
19 (82) Rösner, M.; Haas, S.; Wehling, T. Phase diagram of electron-doped dichalcogenides. *Phys.*
20 *Rev. B* **2014**, *90*, 245105
21
22
23
24 (83) Piatti, E.; Chen, Q.; Tortello, M.; Ye, J. T.; Gonnelli, R. S. Possible charge-density-wave
25 signatures in the anomalous resistivity of Li-intercalated multilayer MoS₂. arXiv:1802.08449
26
27
28
29 (84) Gor'kov, L. P.; Grüner, G. *Charge Density Waves In Solids*, 1st ed.; Elsevier: North Holland,
30 1989; Vol. 25
31
32
33
34 (85) Gonnelli, R. S.; Daghero, D.; Tortello, M.; Ummarino, G. A.; Bukowski, Z.; Karpinski, J.;
35 Reuvekamp, P. G.; Kremer, R. K.; Profeta, G.; Suzuki, K.; Kuroki, K. Fermi-Surface topo-
36 logical phase transition and horizontal Order-Parameter nodes in CaFe₂As₂ under pressure.
37 *Sci. Rep.* **2016**, *6*, 26394
38
39
40
41
42 (86) Allen, P. B.; Dynes, R. Transition temperature of strong-coupled superconductors reanalyzed.
43 *Phys. Rev. B* **1975**, *12*, 905
44
45
46
47
48
49
50
51
52
53
54
55
56
57
58
59
60

E-ph coupling boost ($\Delta\lambda$)